

Article

# Historical aerial surveys map long-term changes of forest cover and structure in the central Congo Basin

Koen Hufkens<sup>1,2,\*</sup>, Thalès de Haulleville<sup>3</sup>, Elizabeth Kearsley<sup>1</sup>, Kim Jacobsen<sup>1,3</sup>, Hans Beeckman<sup>3</sup>, Piet Stoffelen<sup>4</sup>, Filip Vandelook<sup>4</sup>, Sofie Meeus<sup>4</sup>, Michael Amara<sup>5</sup>, Leen Van Hirtum<sup>5</sup>, Jan Van den Bulcke<sup>1</sup>, Hans Verbeeck<sup>1</sup>, Lisa Wingate<sup>2</sup>

<sup>1</sup> Ghent University, Ghent, Belgium;

<sup>2</sup> INRA, UMR ISPA, Villeneuve d'Ornon, France;

<sup>3</sup> Royal Museum for Central Africa, Tervuren, Belgium;

<sup>4</sup> Botanic Garden Meise, Meise, Belgium;

<sup>5</sup> National Archives of Belgium, Brussels, Belgium;

\* Correspondence: koen.hufkens@gmail.com

Version January 24, 2020 submitted to Remote Sens.



**Abstract:** Given the impact of tropical forest disturbances on atmospheric carbon emissions, biodiversity and ecosystem productivity accurate long term reporting of Land-Use and Land-Cover (LULC) change in the pre-satellite era (< 1972) is an imperative. Here, we use a combination of historical (1958) aerial photography and contemporary remote sensing data to map long-term changes in the extent and structure of the tropical forest surrounding Yangambi (DR Congo), in the central Congo Basin. Our study leveraged Structure-from-Motion and a novel Convolutional Neural Network based LULC classifier, using synthetic landscapes based image augmentation, to map historical forest cover across a large sub meter resolution orthomosaic (~82800 ha) geo-referenced to  $\sim 4.7 \pm 4.3$  m. A comparison with contemporary LULC data showed a shift from previously highly regular industrial deforestation of large areas, to discrete smallholder farming clearing, increasing landscape fragmentation but also providing opportunities for substantial forest regrowth. Efforts to quantify long term canopy texture changes and a link to above ground carbon had limited to no success. Our analysis provides methods and insights into key spatial and temporal patterns of deforestation and reforestation at a multi-decadal scale, providing a historical context for past and ongoing forest research in the area.

**Keywords:** Aerial survey, data recovery, CNN, Deep Learning, SfM, Congo Basin

17    **1. Introduction**

18    Tropical ecosystem services are severely impacted by deforestation and forest degradation [1–  
19    3]. Not only does tropical forest Land-Use and Land-Cover Change (LULCC) constitute 10 to 15%  
20    of the total global carbon emissions [4], changes in forest fragmentation affect the forest structure  
21    and function [5–7]. Strong fragmentation effects decreases the number of large trees along forest  
22    edges [8,9], while species composition and biodiversity are equally negatively affected [10–12].  
23    Estimates show that 31% of carbon emissions are caused by edge effects alone [6].

24    Accurate estimates of LULCC and forest canopy structure are therefore imperative to estimate  
25    carbon emissions and other ecosystem services [1,2]. Remote sensing products have been key  
26    inputs in LULCC assessments as they provide accurate spatial information to help estimate carbon  
27    emissions [1,13]. More so, high resolution aerial images provide scientists tools to monitor forest  
28    extent, structure and carbon emissions as canopy texture is linked to above ground biomass [14–16].  
29    Yet, most of these estimates are limited in time to recent decades [1,2,17,18].

30    Historical estimates of Land-Use and Land-Cover (LULC), in the pre-satellite era (< 1972), exist  
31    but generally rely on non-spatially explicit data (i.e socio-economic data) [2,17,19,20]. Efforts have  
32    been made to use other geo-spatial data sources such as historical maps [21], declassified CORONA  
33    satellite surveillance data across the US and central Brazil [22] as well as aerial surveys in post  
34    World War II German [23]. Survey data across the African continent is less common, inaccessible  
35    or both. Some studies do exist, as Buitenwerf *et al.* [24] and Hudak and Wessman [25] used aerial  
36    survey images to map vegetation changes in South African savannas, whilst Frankl *et al.* [26] and  
37    Nyssen *et al.* [27] mapped the Ethiopian highlands of 1930's.

38    Across the central Congo Basin most of these historical images were collected within the  
39    context of national cartographic efforts by the “Institut Géographique du Congo Belge” in  
40    Kinshasa (then Léopoldville), DR Congo. Despite the existence of large archives of aerial survey  
41    imagery (Figure 1, Appendix Figure 3), as of yet, no studies have valorized these data. The lack of a  
42    consistent valorization effort is unfortunate as the African rainforest is the second largest on Earth  
43    and covers ~630 million ha, representing up to 66 Pg of carbon storage [28], and currently loses  
44    forest at an increasing pace [29]. Given the impact of LULCC on the structure and functioning of  
45    central African tropical forests, and their influence on both carbon dynamics [30] and biodiversity  
46    [12], accurate long term reporting of historical forest cover warrants more attention [21].

47    Here, we use a combination of historical aerial photography and contemporary remote  
48    sensing data to map long-term changes in the extent and structure of the tropical forest  
49    surrounding Yangambi (DR Congo), in the central Congo Basin, effectively linking the start of the  
50    anthropocene [31] with current assessments. Yangambi was, and remains, a focal center of forest

51 and agricultural research and development in the central Congo Basin. Past research in the region  
52 allows for thorough assessment of land-use and land-cover change from a multi-disciplinary point  
53 of view, confronting us with complex deforestation and land-use patterns.

54 We leverage Structure-from-Motion to generate a large orthomosaic of historical imagery and  
55 develop a Convolutional Neural Network based forest cover mapping approach, based upon a  
56 semi-supervised generated dataset extensively leveraging data augmentation. Our methodology  
57 aims to provides a historical insight into important LULCC spatial patterns in Yangambi, such  
58 as fragmentation and edge complexity. We further contextualize the influence of changes in the  
59 forest's life history on past and current research into Above Ground Carbon (AGC) storage [30]  
60 and biodiversity [12] in the central Congo Basin. Our fast scalable mapping approach for historical  
61 aerial survey data, using limited supervised input, would further support long-term land-use and  
62 land-cover change analysis across the central Congo Basin.

## 63 2. Methods

### 64 2.1. Historical data acquisition

65 Data for the central Congo Basin region, surrounding Kisangani, were collected in several flights  
66 during the dry season of 1958 and 1959 (from 8/01/1958 to 20/02/1958 and from 28/12/1958  
67 to 9/01/1959 respectively, see Appendix Figure 1) to generate topographic maps of the area,  
68 supervised by the "Institut Géographique du Congo Belge" in Kinshasa, DR Congo (then Léopoldville).  
69 Black-and-White infrared images (0.4 - 0.9  $\mu\text{m}$ ) were gathered along flight paths running mostly from  
70 west to east, between 09:00 and 11:00 local time. Along a flight path continuous images were taken  
71 using a Wild Heerburg RC5a (currently Leica Geosystems) with an Avigon lens assembly (114.83mm  
72 / f 5.6, with a 90°view angle) resulting in square photo negatives of 180 by 180 mm. Flights were  
73 flown at an average absolute altitude of ~5200 m above sea level, covering roughly 18 530 km<sup>2</sup> at an  
74 approximate scale of 1/40 000. The use of the integrated autograph system ensured timely acquisition  
75 of pictures with a precise overlap (~1/3) between images. This large overlap between images together  
76 with flight parameters would allow post-processing, using stereographs, to create accurate topographic  
77 maps. Original data from this campaign are stored in the Royal Museum for Central Africa in Tervuren,  
78 Belgium (Figure 1).

### 79 2.2. Site selection

80 We prioritised flight paths and images that contained current day permanent sampling plots,  
81 larger protected areas, and past agricultural and forest research facilities (Figure 2). This selection  
82 provides a comprehensive mapping of the Yangambi area and the life history of the forest surrounding

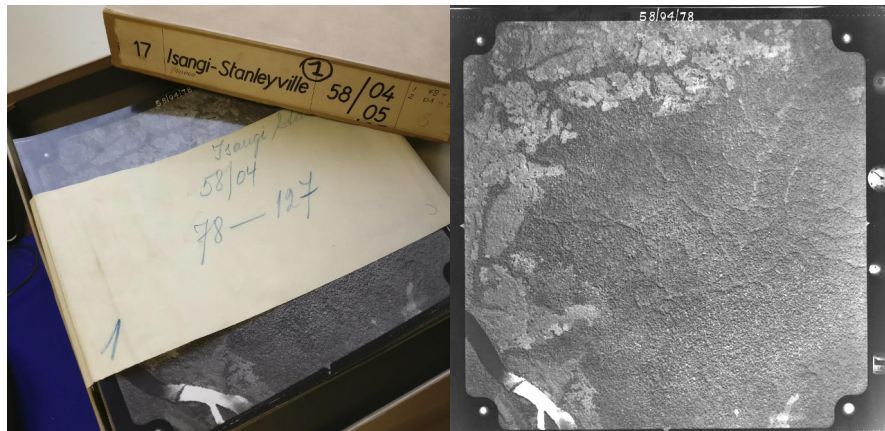


**Figure 1.** A box of historical aerial photographs (left) and a single aerial photograph (right) showing part of the Congo river. Note the meta-data provided in the right side margin of the image, such as acquisition time and flight height.

83 it. Thereafter, we selected flight paths 1 through 11 for digitization. From this larger dataset of 334  
 84 images we selected 74 survey images for orthomosaic compositing and further analysis. All the  
 85 selected images stem from the flight campaign made during January and February of 1958. The area  
 86 includes the Yangambi village, 20 contemporary permanent sampling plots [30], past and present  
 87 agricultural experimental plots [32] and large sections of the Yangambi **UNESCO Man and Biosphere**  
 88 **reserve** surrounding to the west and east of the village. Although not formally mosaicked we provided  
 89 a full dataset of pre-processed images using the cropping and normalization routines described below.  
 90 The latter data was not used in subsequent LULCC analysis, but has been archived and made available  
 91 to the public separately (see code & data availability statement below).

### 92 2.3. Digitization and data processing

93 All selected images, covering the Yangambi area, were contact prints as original negatives of the  
 94 prints were not available. Images were scanned at a resolution exceeding their original resolution  
 95 (or grain) at the maximal physical resolution of an Epson A3 flatbed scanner (i.e. 2400 dpi or 160 MP  
 96 per image) and saved as lossless tiff images. Data were normalized using contrast limited histogram  
 97 equalization [33] with a window size of 32 and a clip limit of 1.5. Fiduciary marks were used to rectify  
 98 and downsample the images into square 7700x7700 pixel images (~1200 dpi, 81 MP). This resulted in a  
 99 dataset with digital images at a resolution that remained above the visible grain of the photographs,  
 100 whilst the reduced image size facilitated easier file handling and processing speed.

101 Data was processed into a georeferenced orthomosaic using a Structure-from-motion (SfM, Ullman  
 102 [34]) approach implemented in **Agisoft Metashape** version 1.5.2 (Agisoft LLC, St. Petersburg, Russia).  
 103 An orthomosaic corrects remote sensing data to represent a perfectly downward looking image, free  
 104 from perspective distortions due to topography and camera tilt. Using the SfM technique features,

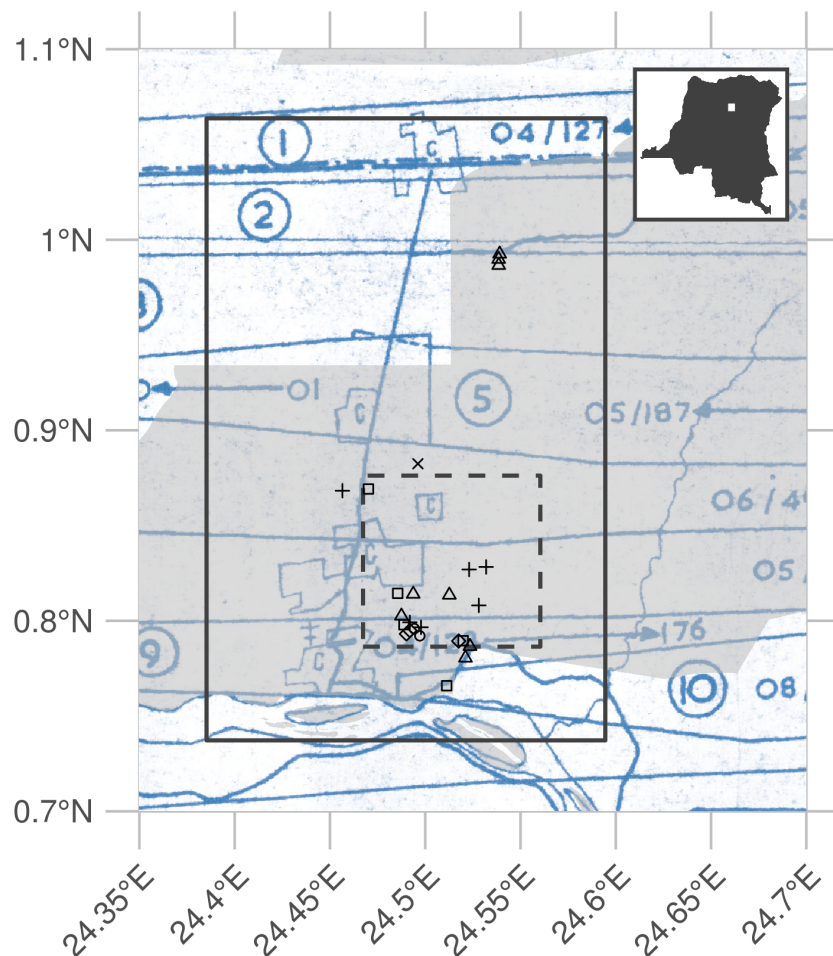


**Figure 2.** Overview of the historical flight paths during aerial photo acquisition and ancillary data used in this study. The bounding box of the orthomosaic data presented in this study is shown as a rectangle (23x36 km). The outline of a recent high-resolution Geo-eye panchromatic image is shown as a dashed dark grey rectangle (10x10km). The location of various permanent sampling plots are shown as x, +, and open squares and triangles for the mixed, mono-dominant and edge plots respectively. The grey polygon delineates the current day Yangambi Man and Biosphere reserve. The inset, top right, situates the greater Yangambi region (white rectangle) with the DR Congo. The full flight plan and details are shown in Appendix Figure 1 and 2

105 areas in images with a large degree of similarity, are matched across various images to reconstruct  
106 a three dimensional scene (topography) from two-dimensional image sequences. During the SfM  
107 analysis we masked clouds, glare or large water bodies such as the Congo river.

108 We calculated the orthomosaic using a low resolution point cloud and digital elevation map  
109 (DEM). Additional ground control points were provided to assist in the referencing of image and  
110 constrain the optimization routine used in the SfM algorithm. Ground control points consisted of  
111 permanent structures which could be verified in both old and new aerial imagery (i.e. ESRI World  
112 Imagery) and consisted of corner points of build structures (e.g. a building, bridge or swimming  
113 pool etc.). Although clouds were removed during the SfM routine we did not mask all clouds in the  
114 final orthomosaic to maximize forest coverage. The final scene was cropped, to provide consistent wall  
115 to wall coverage of the reconstructed scene. The orthomosaic was exported as a geotiff for further  
116 georeferencing in QGIS [35] using the georeferencer plugin (version 3.1.9) and additional ESRI World  
117 Imagery high resolution reference data. We used 3<sup>rd</sup> degree polynomial and 16 ground control points  
118 to correct the final image. Ground control points, raw image data and final processed image are  
119 provided in addition to measures of uncertainty such as mean and median error across all ground  
120 control points. All subsequent analysis are executed on the final geo-referenced orthomosaic or subsets  
121 of it.

122 *2.4. Land-Use and Land-Cover Change*

123 *2.4.1. Classifying Land-Use and Land-Cover*

124 *Model training*

125 We automatically delineated all natural forest in the historical data, thus excluding tree plantations,  
126 thinned or deteriorated forest stands which showed visible canopy cover loss, fields and buildings.  
127 We used the Unet Convolutional Neural Net (CNN, Ronneberger *et al.* [36]) architecture implemented  
128 in Keras [37] with an efficientnetb3 pre-processing backbone [38] running on TensorFlow [39] to train  
129 a binary classifier (i.e. forest or non-forested). Training data were collected from the orthomosaic by  
130 randomly selecting 513 pixel square tiles from locations within homogeneous forested or non-forested  
131 polygons in the historical orthomosaic (Figure 5). Separate polygons were selected for training,  
132 testing and validation purposes. Validation polygons were sampled 300 times, while both testing  
133 and validation polygons were sampled at 100 random locations. Tiles extracted from locations  
134 close to the polygon border at times contained mixed cover types. Tiles with mixed cover types  
135 were removed from the list of source tiles (Table 1). Homogeneous source tiles were combined in  
136 synthetic landscapes using a random gaussian field based binary mask (Figure 3). We generated 5000

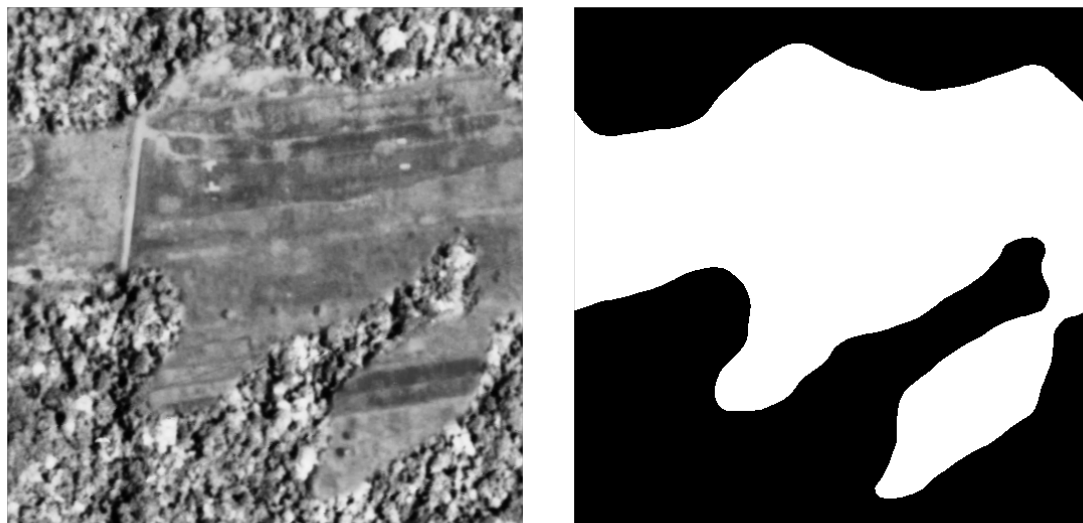


**Figure 3.** An example synthetic landscape, combining homogeneous forest and non-forest images into a patchy landscape using random gaussian field based masks. The left panel shows a combined synthetic landscape, while the right panel shows the corresponding forest (black) and non-forest (white) labels.

137 synthetic landscapes (**balancing forest and non-forest classes**) for training, while 500 landscapes were  
 138 generated for both the validation and the testing datasets for a total of 6000 synthetic landscapes. In  
 139 order to limit stitch line misclassifications, along the seams of mosaicked images, we created synthetic  
 140 landscapes with different forest tiles to mimick forest texture transitions. We applied this technique to  
 141 10% of the generated synthetic landscapes (**across training, validation and testing data**).

**Table 1.** Number of source tiles used for the generation of synthetic landscapes.

	training	testing	validation
forest	300	100	100
non-forest	294	92	84

142 The CNN model was trained for 100 epochs with a batch size of 30 using Adam optimization [40],  
 143 maximizing the Intersect-over-Union (IoU) using Sørensen–Dice [41] and categorical cross-entropy  
 144 loss functions. Data augmentation included random cropping to 320 pixel squares, random orientation,  
 145 scaling, perspective, contrast and brightness shifts and image blurring. The optimized model was used  
 146 to classify the complete orthomosaic using a moving window approach with a step size of 110 pixels  
 147 and a majority vote (> 50% agreement) across overlapping areas to limit segmentation edge effects.  
 148 **In addition, we provide raw pixel level classification agreement data for quality control purposes**  
 149 **(see Data availability below)**. We refer to Figure 4 for a synoptic overview of the full deep learning  
 150 workflow.

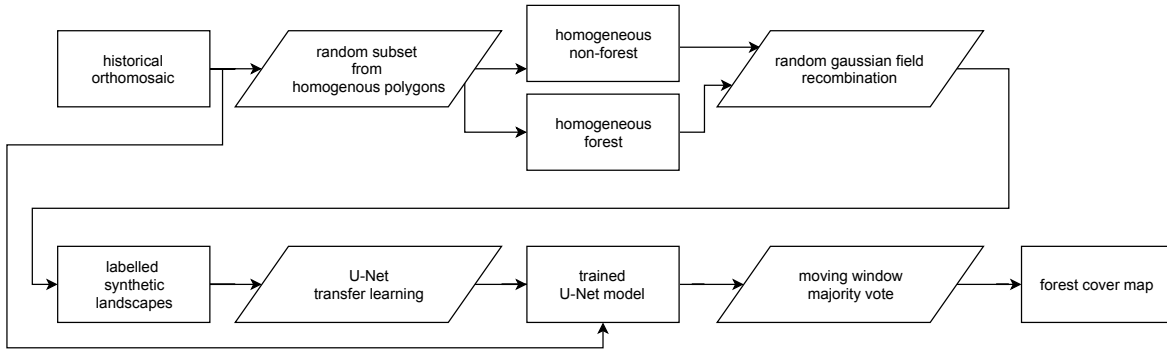


**Figure 4.** A diagram of the deep learning workflow followed in training a binary forest / non-forest cover convolutional neural net U-Net model to generate our forest cover map.

151 *Model validation*

152 We report the CNN accuracy based upon the IoU of our out-of-sample validation dataset  
 153 of synthetic landscapes. In addition, we report confusion matrices for all pixels across the  
 154 homogeneous validation polygons, as well as the training and testing polygons (see Figure  
 155 5). Furthermore, we used the first acquisition of a recent pan-chromatic Geo-Eye 1 stereo pair  
 156 (Geo-Eye, Thornton, Colorado, U.S.A., order 737537, 2011-11-11 08:55 GMT or 09:55 local time)  
 157 to classify and assess the robustness of the CNN algorithm on contemporary remote sensing  
 158 imagery with similar spectral and spatial characteristics. We used the Global Forest Change  
 159 version 1.6 (GFC, tile 10N-020E) [1] map data, capturing forest loss up to 2011, to quantify accuracy  
 160 on downsampled CNN Geo-Eye classification results. Once more, we report the confusion matrix  
 161 of between the GFC and CNN derived forest cover maps, masking clouds and cloud shadows. To  
 162 summarize confusion matrices we report accuracy as:

$$163 \quad Accuracy = \frac{(TP+TN)}{(TP+TN+FP+FN)}$$

164 in which TP, TN, FP, FN are True Positive, True Negative, False Positive and False Negative,  
 165 respectively.

166 2.4.2. Characterizing long term change

167 To map long term LULCC in the Yangambi region we used the contemporary Global Forest  
 168 Change version 1.6 (GFC, tile 10N-020E) map data [1]. Using the GFC data we calculated the latest  
 169 state of the forest with respect to the conditions at the start of 1958, 60 years earlier. In our analysis we  
 170 only included GFC pixels which recorded no forest loss throughout the whole 2000 - 2018 period. As  
 171 the resolution of the historical forest classification exceeds that of the GFC map we downsampled our  
 172 historical forest cover data to 30 m GFC resolution **using a nearest neighbour approach**. We masked  
 173 out all water bodies using the Global Forest Change survey data mask layer, and limited the analysis  
 174 to the right bank of the Congo river. We provide summary statistics of historical and contemporary

175 forest loss and regrowth. We map persistent forest loss after 1958, regrowth after loss in 1958, recent  
176 forest loss and long term (stable) forest cover.

177 2.4.3. Landscape fragmentation & Above Ground Carbon estimates

178 To quantify changes in the structure of forest cover and its disturbances we used spatial  
179 pattern analysis landscape (fragmentation) metrics [42]. Landscape metrics provide a mathematical  
180 framework for the analysis of discrete land-cover classes and allows us to capture their  
181 composition and configuration. These metrics are therefore commonly used to compare how  
182 landscapes change over time [43]. In particular, fractals provide a way to quantify complex natural  
183 landscapes, including their self-similarity, across scales [44,45] We report the ratio of edge to area  
184 and the fractal dimension to quantify landscape complexity of forest disturbances. A fractal dimension  
185 closer to 2 suggest a more complex (fragmented) landscape.

186 Statistics were calculated for all forest disturbance patches larger than 1 ha and smaller than the  
187 95<sup>th</sup> percentile of the patch size distribution using the R package landscapemetrics [43]. We provide  
188 mean and standard deviation on edge, area, their ratio and fractal dimension for both the historical  
189 and contemporary Hansen *et al.* [1] forest cover maps.

190 We estimated above ground carbon (AGC) losses and gains over time using plot based averages  
191 of recent inventory data at permanent sampling plots in the area (Figure 2). We refer to Kearsley *et al.*  
192 [30] for the survey method and allometric relations used to scale the survey data. Unlike standard  
193 square 1 ha plots, edge plots were set back 200 m from forest edges and were 50x200 m, with the  
194 50 m side of the plot along the forest edge and continuing 200 m into the forest (Appendix Table 1).  
195 We further confirmed that forest edge plots did not show a significantly different AGC compared to  
196 those of non-edged / mixed forest plots (Mann Whitney U test,  $p < 0.05$ ). Thus it was not necessary to  
197 explicitly quantify changes in AGC caused by edge effects. Moreover, we used the mean values of the  
198 mixed forest as representative for potential AGC losses. Despite the challenges inherent in quantifying  
199 AGC for forest edges we mapped the total extent of the edges in the contemporary landscape. To  
200 align our landscape analysis with exploratory analysis of the survey data we used a buffer of 200 m to  
201 estimate the extent of forest edges and patches, up to the location of forest edge plots.

202 Surveys of old plantations show a large variation in AGC, depending on age and the crop type.  
203 For example, the AGC values varied from 168.67 to 86.55 Mg C ha<sup>-1</sup>, for *Hevea brasiliensis* (rubber  
204 tree) and *Elaeis guineensis* (oil palm) plots respectively (Bustillo *et al.* [46], personal communications).  
205 These higher values are in line with the mixed AGC estimates in the area, while the palm plantations  
206 resemble old-regrowth values (81.8 Mg C ha<sup>-1</sup>, see Appendix Table 1). We therefore use both the

207 estimates of old-regrowth and mixed forest to estimate AGC for regrowth. We did not have sufficient  
208 data to account for individual changes in AGC across plantations.

209 *2.5. Canopy structure & FOTO texture analysis*

210 We compared the structure of the canopy both visually and using Fourier Transform Textural  
211 Ordination (FOTO, Couteron [47]). FOTO uses a principal component analysis (PCA) on radially  
212 averaged 2D Fourier spectra to characterize canopy (image) texture. The FOTO technique was first  
213 described by Couteron [47] to quantify canopy stucture in relation to biomass and biodiversity, and  
214 can be used across multiple scenes using normalization [16].

215 We used the standard FOTO methodology with fixed zones, instead of the moving window  
216 approach. The window size was set to the same size (187 pixels or ~150 m) as used in the moving  
217 window analysis above. To account for illumination differences between the two scenes we applied  
218 histogram matching. No global normalization was applied, as the scene was processed as a whole. PC  
219 values from this analysis for all permanent sampling plots in both image scences were extracted using  
220 a buffer with a radius of 50 m.

221 For both site based and scene analysis we correlated PC values with permanent sample plot  
222 inventory data such as stem density, above ground biomass and tree species richness. Additional  
223 comparisons are made between contemporary Geo-Eye data and the historical orthomosaic derived PC  
224 values. Due to the few available permanent sampling plots in both scenes we used a non-parametric  
225 paired signed rank (Wilcoxon) test [48] to determine differences between the PC values of the Geo-Eye  
226 and historical orthomosaic image scenes across mono-dominant and mixed forest types. In all analysis,  
227 mono-dominant site 4 was removed from the analysis due to cloud contamination.

228 **3. Results**

229 *3.1. Orthomosaic construction*

230 Our analysis provides a first spatially explicity historical composite of aerial survey images **in**  
231 **support of mapping land-use and land-cover** within the Congo Basin. The use of high resolution  
232 historical images combined with SfM image processing techniques allowed us to mosaic old imagery  
233 across a large extent. The final orthomosaic composition of the Yangambi region **provided** an image  
234 scene covering approximately 733 million pixels across ~82800 ha (~23x36 km, Figure 2). The overall  
235 accuracy of the SfM orthomosaic composition was 0.88 m/pixel using the sparse cloud DEM for  
236 corrections at 45.8 m/pixel. The resulting georeferenced scene had a spatial accuracy of approximately  
237 **23 m**. Further georeferencing outside the SfM workflow reduced the mean error at the ground control  
238 points to  $5.3 \pm 4.9$  px ( $\sim 4.7 \pm 4.3$  m), with a median error of 2.9 px (2.6 m). The orthomosaic served

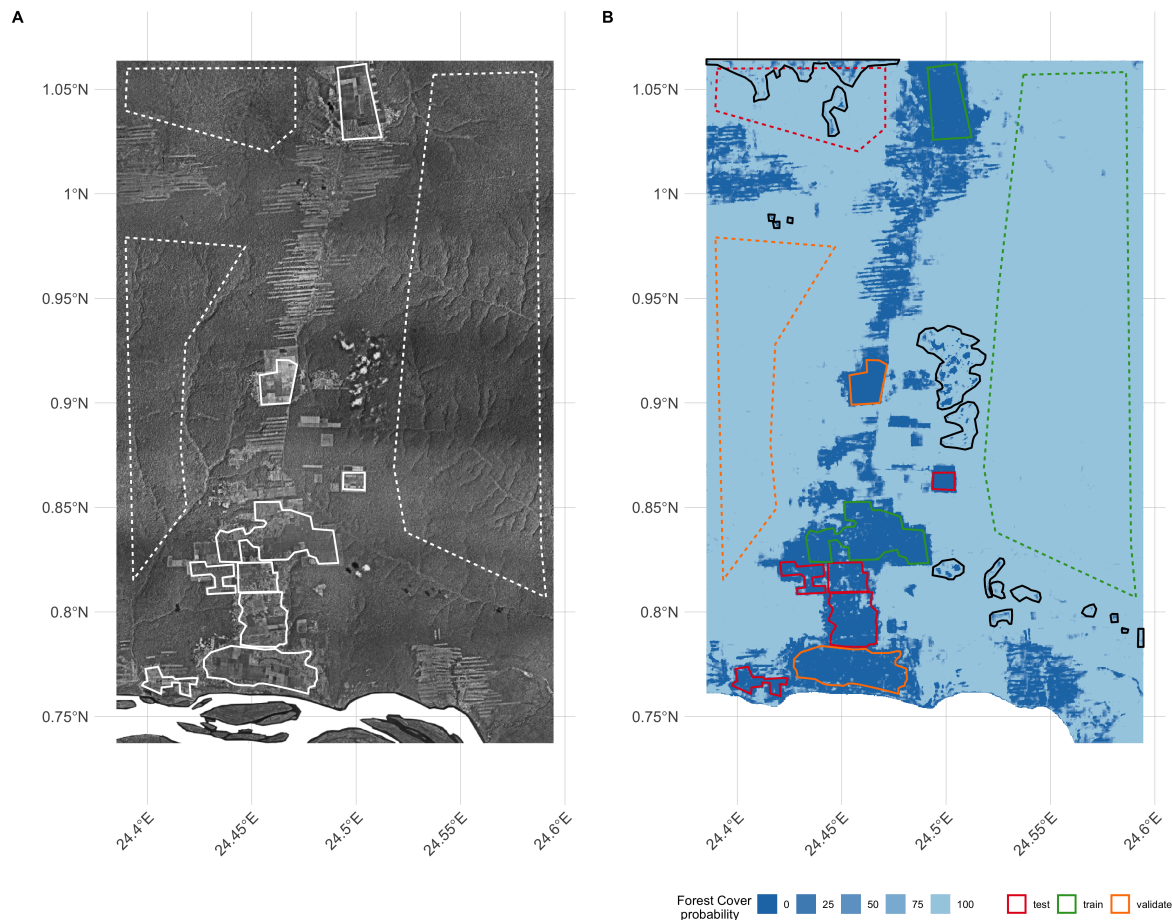


**Figure 5.** Overview of the final orthomosaic of the greater Yangambi region (A) as well as the forest cover classification uncertainty (B) used to generate the final Land Land Cover map (see Figure 6). Homogeneous polygons used in the generation of the synthetic landscape for Convolutional Neural Network training, testing and validation are marked as dashed and full lines for forest and non-forest regions, respectively. Training, testing and validation regions are denoted in panel B in green, red and orange, respectively. Black polygon outlines denote cloud and image stitch line regions which were manually excluded from analysis, but retained in calculation of validation statistics (see Table 2).

as input for all subsequent LULCC analysis with all derived maps provided with the manuscript repository (see data & code availability statements below).

### 3.2. Land-use and Land-Cover Classification

#### 3.2.1. CNN model validation

The CNN deep learning classifier reached an Intersection-over-Union accuracy of 97% on the detection of disturbed forest in the out-of-sample (validation) synthetic landscape data. Using all pixels within the validation polygons (Figure 5) showed a similar accuracy value of ~98%. Using all polygons across the scene, including those used in the generation of testing and training synthetic landscapes, increased the accuracy to ~99% (Table 2). A comparison with recent pan-chromatic

<sup>248</sup> **Geo-Eye data shows good agreement, with an accuracy of ~87% across all pixels, between the**  
<sup>249</sup> **landsat based GFC data and downscaled CNN results (Table 2 and Figure 7).**

**Table 2.** Confusion matrix showing % agreement between forest / non-forest classes using a Convolutional Neural Network (CNN) across previously selected homogenous areas.

CNN	Geo-Eye (full scene)		Aerial Survey (all polygons)		Aerial Survey (validation polygons)	
	non-forest	forest	non-forest	forest	non-forest	forest
non-forest	10.17	8.55	97.4	0.19	98.59	0.0
forest	3.75	77.52	2.6	99.81	1.41	100.0
<b>Accuracy</b>		87.70		98.61		99.3

<sup>250</sup> *3.3. Long term changes in LULC and Above Ground Carbon*

<sup>251</sup> Scaling our classifier to the whole historical orthomosaic we detected **~16200 ha** (or ~20% of the  
<sup>252</sup> scene) of disturbed forests. A large fraction of the disturbed area was restored in the period between  
<sup>253</sup> the two **acquisition periods**. In total, **9918 ha**, or little over half of the affected forest was restored  
<sup>254</sup> (Figure 5C-D, dark blue). Recent deforested areas, as registered through satellite remote sensing,  
<sup>255</sup> approximate **8776 ha** (**Table 3, Figure 6 - light green**).

<sup>256</sup> Recent deforestation follows a distinctly different pattern compared to historical patterns.  
<sup>257</sup> Historical deforestation showed a classical fishbone pattern for forest clearing with very sharp edges,  
<sup>258</sup> while current patterns are patchy and ad-hoc (**figure 6C**, dark blue and green colours respectively).  
<sup>259</sup> These differences are reflected in the analysis of landscape metrics of forest loss. Between the historical  
<sup>260</sup> and contemporary LULCC maps we see an increase in small disturbances, as indicated by the  
<sup>261</sup> decreasing area of the mean patch size, down to  $\sim 1.86 \pm 0.75$  ha from  $\sim 5.25 \pm 5.02$  ha historically.  
<sup>262</sup> Perimeter lengths were longer historically, at  $1451 \pm 943$  m, compared to contemporary landscapes  
<sup>263</sup>  $\sim 921 \pm 362$  m (Table 3). This shift in perimeter area ratio led to a similar change in the fractal index,  
<sup>264</sup> slightly increasing in value to  $1.1 \pm 0.05$  from  $1.09 \pm 0.04$  over time. Values closer to a fractal index of  
<sup>265</sup> 2 suggest a more complex (fragmented) landscape.

<sup>266</sup> A comparison of forest edge plots with mixed forest plots showed no significant difference in  
<sup>267</sup> AGC, or other reported values such as species richness, basal area or stem density (Mann Whitney U  
<sup>268</sup> test,  $p < 0.05$ ). Edge influence did not extend beyond 200 m from a forest edge, but still represented an  
<sup>269</sup> area of **13151 ha**.

<sup>270</sup> Changes in both land-use and land-cover led to concomitant changes in AGC stocks. Recovery  
<sup>271</sup> throughout the region was characterized for patches of forest and plantations. Assuming high density  
<sup>272</sup> stands, based on previous work, this could amount to a carbon gains of 1592 Gg C across our study  
<sup>273</sup> area, offsetting more recent losses of approximately 1408 Gg C. On the other hand, at the low end, if  
<sup>274</sup> we assume a lower carbon density of  $81.8 \text{ Mg C ha}^{-1}$  this would result in a total carbon gain of 811 Gg

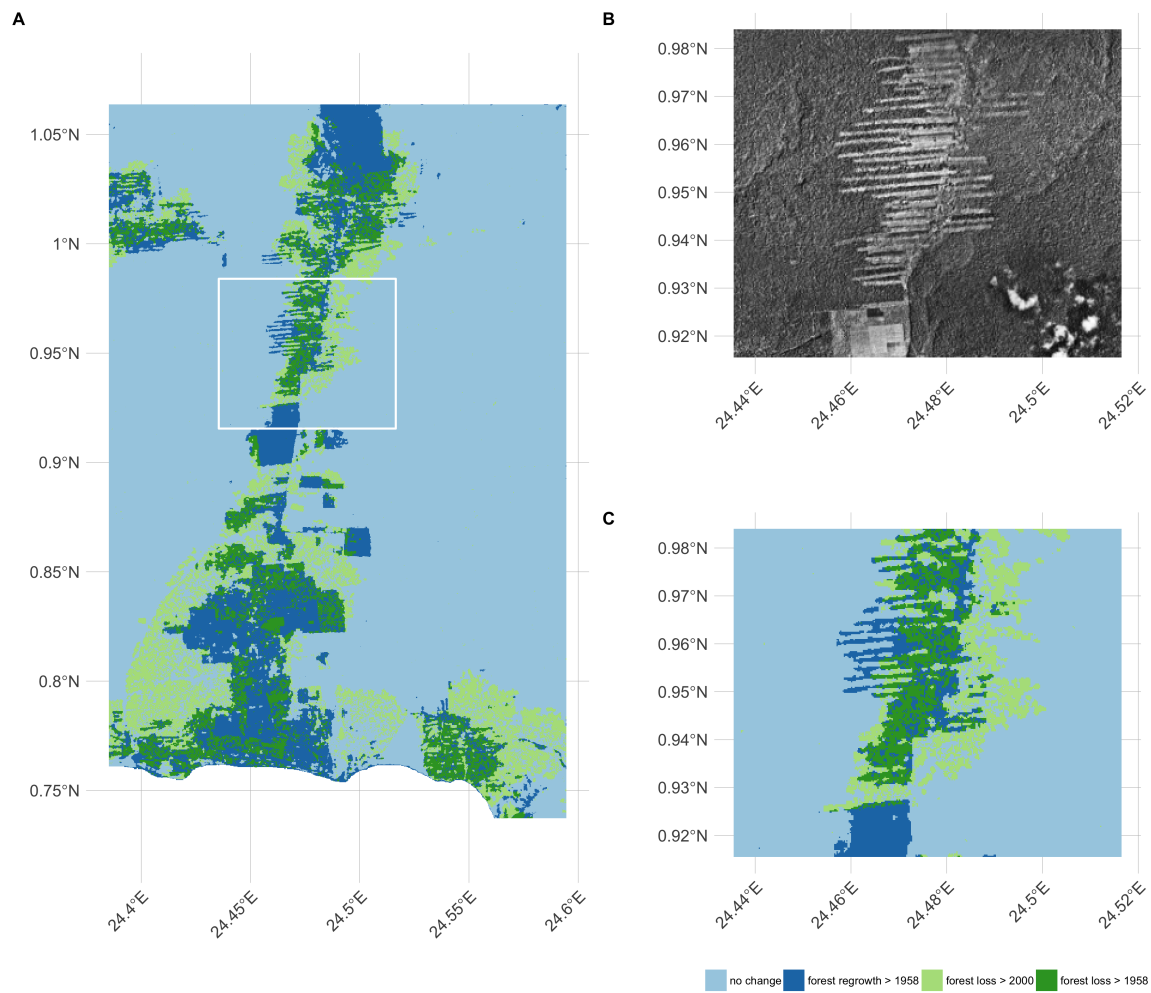


**Figure 6.** Overview of the final Land Use Land Cover Change map, a detailed inset of both the underlying orthomosaic (B) and the derived land use land cover change map displayed as the difference between the Convolutional Neural Network based classification orthomosaic and the recent Landsat based forest cover map by Hansen et al. 2013 (C).

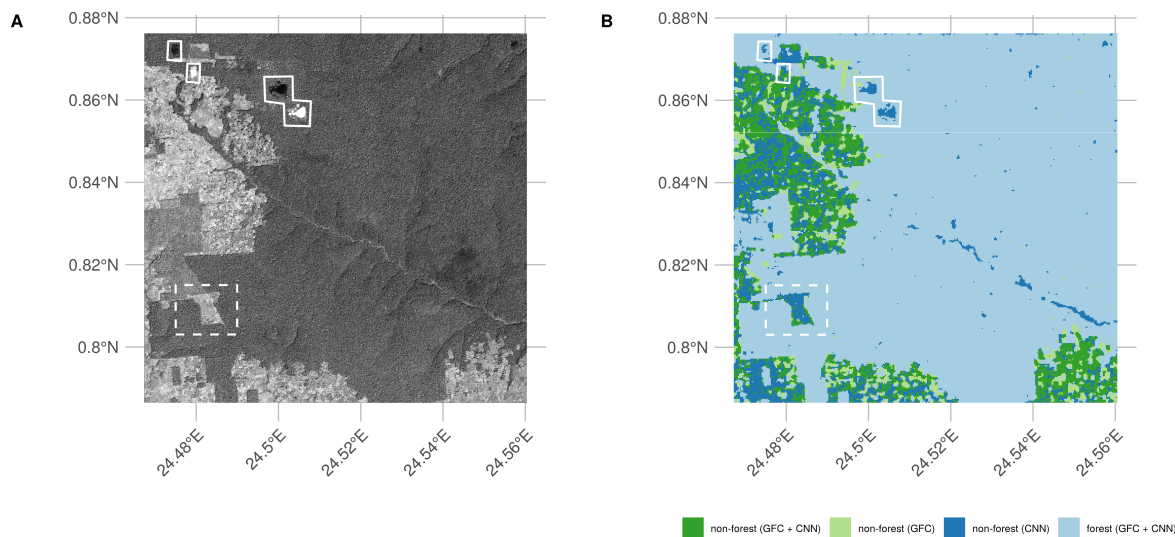


**Figure 7.** Convolutional Neural Network (CNN) based forest cover classification results (B) as run on a recent (2011) Geo-Eye panchromatic image (A). We show the difference between the Convolutional Neural Network based classification and a recent Landsat based forest cover map by Hansen et al. 2013. Full white outlines denote cloud contamination, the dashed rectangle shows a location where the CNN outperforms the Landsat based forest classification.

275 C. Using our approach results indicate that overall deforestation around Yangambi has resulted in a  
 276 loss of ~2416 Gg C in AGC stocks.

**Table 3.** Land use land cover change statistics of forest cover around Yangambi in the central Congo Basin. The data evaluates a difference between a historical (1958) aerial photography based survey and the Hansen et al. 2013 based satellite remote sensing data. Spatial coverage statistics are provided in square kilometers (km) and hectares (ha), rounded to the nearest integer as well as Above Ground Carbon (AGC) scaled using recent survey measurements.

	AGC	
	ha	Gg C ha <sup>-1</sup>
Forest	68455	
- of which edges	13151	
Regrowth > 1958 loss	9918	811 - 1592
Loss > 2000	8776	1408
Loss > 1958 (permanent)	6282	1008

**Table 4.** Landscape metrics for historical and contemporary deforestation patterns. We report patch perimeter and area, their ratio and fractal dimension. Values are reported as mean ± standard deviation, across all deforestation patches.

	perimeter (m)	area (ha)	ratio ( $m^{-1}$ )	fractal dimension
historical	1451.58 ± 943.27	5.25 ± 5.02	0.03 ± 0.01	1.09 ± 0.04
contemporary	921.74 ± 362.59	1.86 ± 0.75	0.05 ± 0.01	1.1 ± 0.05

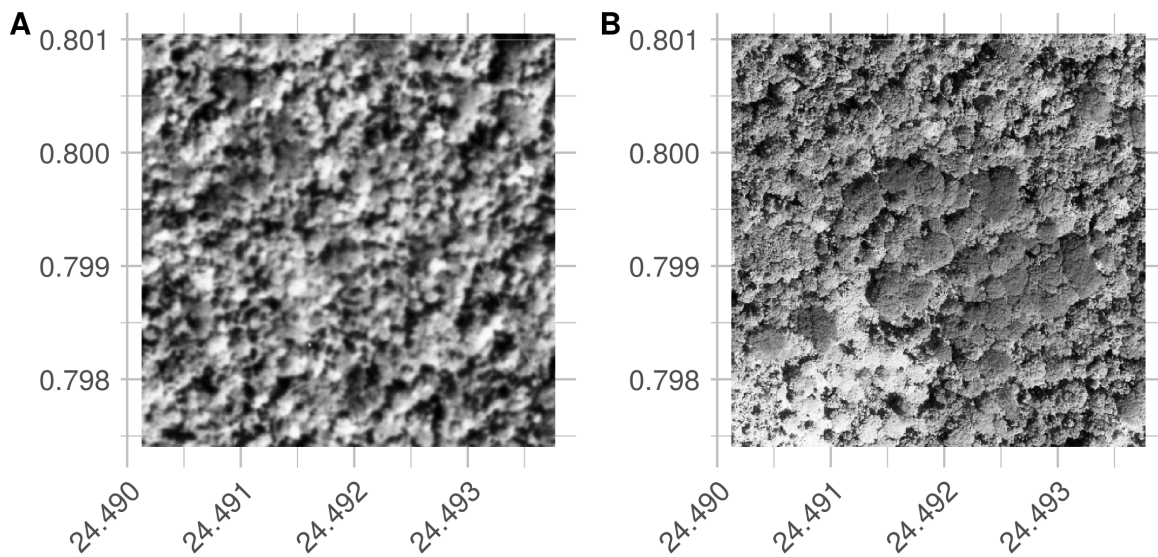


**Figure 8.** Visual comparison between a historical (A) and contemporary (B) permanent sampling plot. The site is currently listed as a mono-dominant *Brachystegia laurentii* stand. Note the structural differences with a 'coarser' canopy structure in the historical image compared to the more closed contemporary stand.

<sup>277</sup> *3.4. Canopy structure & FOTO texture analysis*

<sup>278</sup> Visual interpretation of the scenes provide evidence that most locations do not change dramatically  
<sup>279</sup> with respect to canopy composition, except for the large areas of disturbances in contemporary fallow  
<sup>280</sup> or young-regrowth plots. One marked difference is noted in the mono-dominant plot 6 (Appendix  
<sup>281</sup> Table 1). Here, the current mono-dominant *Brachystegia laurentii* is a recent development, changing  
<sup>282</sup> the canopy structure visibly during the last half century (**Figure 8**). The previous varied canopy  
<sup>283</sup> structure gave way to a more dense and uniform canopy. This is reflected in a change of the FOTO PC  
<sup>284</sup> value from 0.19 historically to its current value of 0.54. This historical value is similar to the mean of  
<sup>285</sup> contemporary mono-dominant stands of *Gilbertiodendron dewevrei* with PC averaging  $0.34 \pm 0.1$ , and is  
<sup>286</sup> only slightly higher than historical values for a mixed forest ( $0.18 \pm 0.08$ ). The reverse pattern is seen  
<sup>287</sup> in the contemporary PC values. Here, the value of 0.54 exceeds those of most mono-dominant stands  
<sup>288</sup> ( $0.35 \pm 0.08$ ), and is even further removed from the values noted for mixed forests ( $0.12 \pm 0.03$ ).

<sup>289</sup> Using only small subsets around existing permanent sampling plots we show distinct differences  
<sup>290</sup> between forest types, with PC values in both historical and contemporary imagery markedly higher  
<sup>291</sup> for the mono-dominant forest types compared to all others (**Appendix Figure 4**). Provided that the  
<sup>292</sup> young-regrowth and fallow permanent sampling plots have seen recent disturbance the Wilcoxon  
<sup>293</sup> signed rank test on the mixed and mono-dominant plots between the historical and contemporary  
<sup>294</sup> PC values did not show a significant difference ( $p > 0.05$ ). Similarly, no significant different using  
<sup>295</sup> PC values extracted from the whole scene analysis was noted ( $p > 0.05$ ). Any relationships between

296 contemporary Geo-Eye data and permanent sampling plot measurements of Above Ground Carbon,  
297 stem density and species richness were non-significant ( $p > 0.05$ , Appendix **Figures 5-7**).

298 Furthermore, visual inspection of the scene wide analysis suggests historical scenes do not show  
299 landscape wide canopy features (**Figure 9 A-B**), unlike the contemporary scene (**Figure 9 C-D**). Where  
300 the FOTO algorithm picks up landscape features such as changes in texture across the contemporary  
301 Geo-Eye scene (e.g. the river valley as a diagonal line in **Figure 9D**), however, no corresponding  
302 landscape patterns are found by the FOTO algorithm in the historical orthomosaic.

303 **4. Discussion**

304 Finely grained spatial data sources, such as remote sensing imagery, are rare before the satellite era  
305 (<1972). This lack of data limits our understanding of how forest structure has varied over longer time  
306 periods in remote areas. Long term assessment can be extended by using large inventories of historical  
307 aerial survey data [22,23,49]. Despite the difficulties in recovering this data and its limitations, such  
308 as invisible disturbances [50], remote sensing generally remains the best way to map and quantify  
309 LULCC [2]. In our study we used novel numerical remote sensing techniques to valorize, for the  
310 first time, historical remote sensing data in order to quantify (long term) land-use and land-cover  
311 change and canopy structural properties in the central Congo Basin. Despite these successes some  
312 methodological and research considerations remain.

313 *4.1. Methodological considerations*

314 *4.1.1. Data recovery challenges*

315 In our study the archive data recovered was limited to contact prints and therefore did not  
316 represent the true resolution of the original negative. In addition, analogue photography clearly  
317 produces a distinct softness compared to digital imagery (**Figure 8**). Despite favourable nadir image  
318 acquisitions [51] image softness combined with illumination effects between flight paths, and the  
319 self-similar nature of vast canopy expanses [52–54], limited our ability to provide wall-to-wall  
320 coverage of the entire dataset containing 334 images. Few man made features in the scenes also  
321 made georeferencing challenging. Although the village of Yangambi provided a range of buildings  
322 as (hard-edge) references, other areas within the central Congo Basin might have fewer permanent  
323 structures and would require the use of soft-edged landscape features (e.g. trees, river outflows).  
324 Research has shown that soft-edged features can help georeference scenes even when containing few  
325 man-made features [55]. Our two step georeferencing approach resulted in a referencing accuracy of  
326  $\sim 4.7 \pm 4.3$  m across reference points. However, it shoud be noted that referencing accuracy of the final  
327 scene is less constrained toward the edges of the scene.

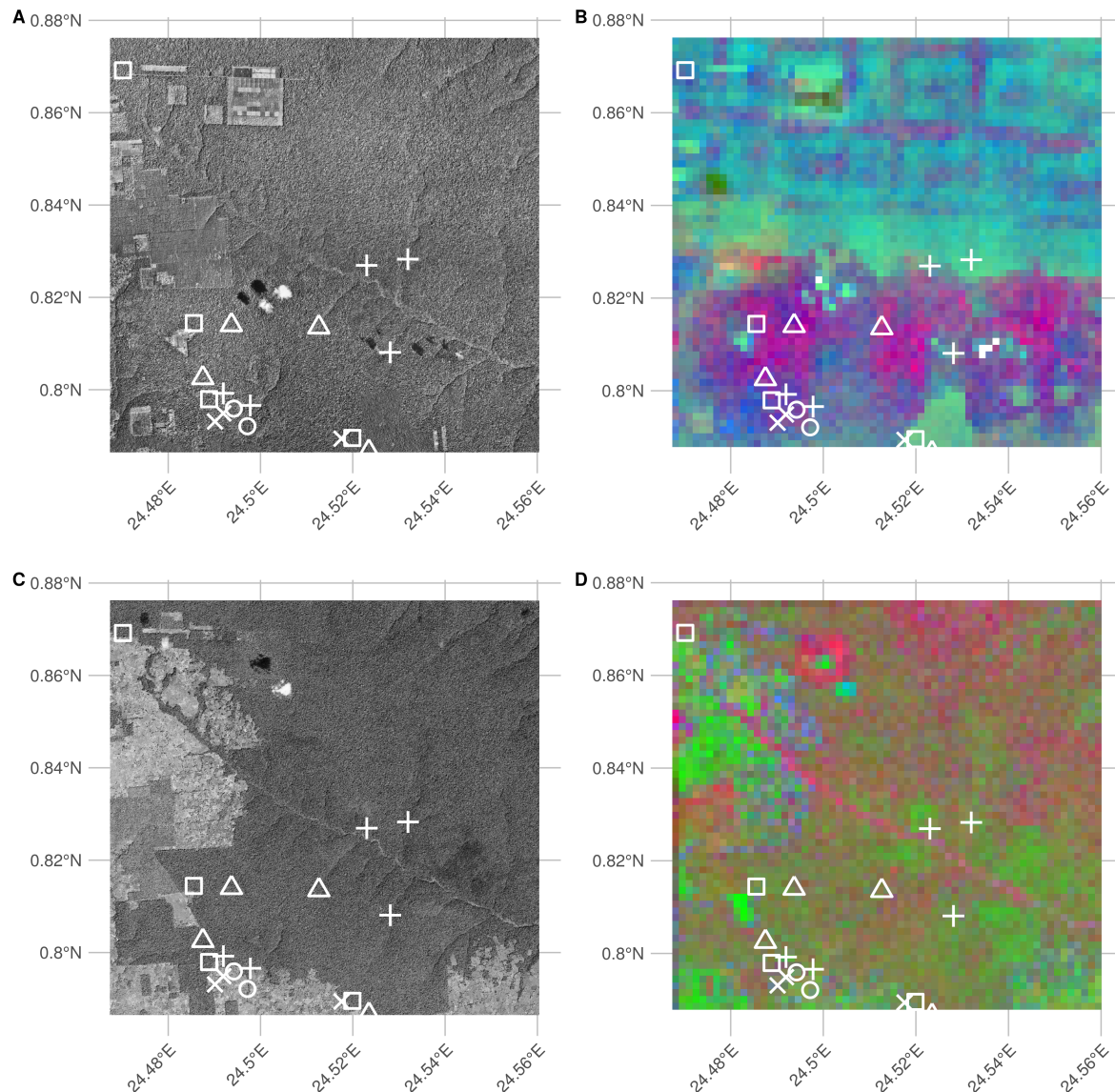


**Figure 9.** RGB visualizations of the first three principal components of scene wide FOTO texture analysis of historical and current (Geo-Eye) imagery. Current permanent sampling plots of mono-dominant, mixed, fallow and young (edge) forest plots are marked with open triangles, open circles, open squares and crosses, respectively.

328 4.1.2. LULC classification & validation

329 When classifying the orthomosaic into forest and non-forest states we favoured a deep  
330 learning supervised classification using a CNN over manual segmentation to guarantee an  
331 “apples-to-apples” comparison between the historical and the contemporary GFC forest cover map  
332 used in our analysis. We acknowledge that both the CNN and GFC land-use and land-cover maps  
333 use different underlying features, i.e. spatial or spectral data, yet attain a similarly high accuracy  
334 of up to 99% [1]. More so, when validating our CNN classifier against GFC data (Figure 7) for a  
335 contemporary high resolution Geo-Eye panchromatic image we reach an accuracy of ~87%, despite  
336 a time difference of almost 60 years. Visual inspection of the classification data in Figure 7 suggests  
337 that the GFC map more often than not classifies non-forest areas as forest. Actual classification  
338 accuracy of our algorithm might therefore be higher than our reported value.

339 4.1.3. Scaling opportunities

340 Our approach uses broadly defined homogeneous polygons to construct a balanced dataset of  
341 synthetic landscapes. The methodology is analogous to the use of sparse labelling as used by  
342 Buscombe and Ritchie [56] and contrasts with the standard methodologies which generally extract  
343 pixel (windows) [22] or delineate land cover classes [23] to drive a classifier or analysis. More  
344 so, the use of heavy image augmentation during model training sidesteps texture representation  
345 issues which affect classification of image scenes with inconsistent illumination or sharpness [25]  
346 or ad-hoc feature engineering [22]. The use of synthetic landscapes allowed us to account for most,  
347 but not all, of the variability within our orthomosaic. Our analysis has shown that despite being  
348 trained on historical data our model could map contemporary forest cover in remote sensing data  
349 with similar spatial and spectral characteristics (Figure 7), suggesting that the classifier consistently  
350 works across both space and time. We acknowledge that the use of synthetic landscapes is limited  
351 by the available homogeneous areas to sample from and the number of classes. Yet, the latter  
352 should not be a constraint as previous research efforts have focussed on simple forest loss maps  
353 [1].

354 4.2. Research context

355 4.2.1. Long term changes in LULC and Above Ground Carbon

356 Our analysis shows that the majority of deforestation around Yangambi happened toward the late  
357 1950’s (~16200 ha). Considerable regrowth has occurred since the aerial survey was executed (~9918  
358 ha), and socio-economic instability prevented further large scale forest exploitation. In particular, many  
359 plantations have reached maturity and forest has re-established in previously cleared or disturbed

360 areas. The majority of this forest recovery takes the form of isolated patches of forest but is offset  
361 by further deforestation of previously untouched forest. Generally, the function and structure of  
362 forests can be influenced by forest edges that are located up to 1km away however most effects are  
363 pronounced within the first 300 m from the edge [57]. Our analysis of edge effects on AGC has shown  
364 that the influence is negligible 200 m away from the edge. Phillips *et al.* [58] have shown similar weak  
365 responses to edge effects in the Amazon forest. Due to a lack of data on the extent (depth) of edge  
366 effects and their influence on AGC beyond 200 m we did not include any estimates of carbon loss  
367 or gain within these zones. However, it must be stated that the influence of edges throughout the  
368 landscape was not marginal as these areas would account for **13151 ha**. Thus edges could have a  
369 substantial negative [6] or positive [59] influence on AGC. Similarly, uncertainties in how to explicitly  
370 correct for plantations in the landscape present a further challenge. Thus, although our estimates  
371 are only indicative they do underscore the important influence of landscape structure when carbon  
372 accounting. However, our findings do not indicate that deforestation in Congo basin is declining, on  
373 the contrary.

374 Over the past half century there has been a clear shift in land use in Yangambi (Figure 5). Land  
375 use has shifted away from for example a regular fishbone deforestation pattern that emerges when  
376 (large scale) agricultural interests dominate the landscape [60], to a more fragmented landscape  
377 (Figure 5D). The former is consistent with historical land management at the time of the aerial  
378 survey [46]. These regular patterns have since been reversed because of a decrease in large scale  
379 intensive agriculture, replaced by ad-hoc small scale subsistence farming with large perimeter to area  
380 relationships (i.e. ragged edges). Consequently, edge effects in the current landscape are far more  
381 pronounced than in the historical scene.

382 Visual inspection of the images also suggests that reforestation within the historically cleared areas  
383 and experimental plots is not necessarily limited to areas far removed from more densely populated  
384 areas. For example, large reforested areas exist close to the Congo stream and Yangambi village itself  
385 (Fig. 5). Here, regional political components, such as land leases and large scale ownership could  
386 have played a role in safeguarding some of these areas for rewilling or sustainable management  
387 [61,62]. Despite widespread anthropogenic influences throughout the tropics [31] the retention of  
388 these forested areas show the potential of explicit or implicit protective policy measures (e.g. INERA  
389 concessions, Bustillo *et al.* [46]) on a multi-decadal time scale. Forest regrowth in non-continuous areas  
390 within Yangambi could increase landscape connectivity and help increase biodiversity [12].

391 Our analysis therefore provides an opportunity to highlight and study those regions that have  
392 previously suffered confirmed long-term disturbances, and those that have been restored since.  
393 Assessments of old plantations and recovering clear-cut forests can serve as a guide to help estimate

394 carbon storage capacity and forest recovery rates in managed and unmanaged conditions [18,20,63]  
395 over the mid- to long-term, in support of rewilding and general forest restoration [12,61,62]. In addition,  
396 mapping long-term edge effects can further support research into issues such as receding forest edges  
397 [57].

398 4.2.2. Canopy structure & FOTO texture analysis

399 Finally, the FOTO technique used to quantify relationships between canopy structure and forest  
400 characteristics rendered no valuable insights of either the historical orthomosaic or recent Geo-Eye  
401 scene. Similarly weak correlations were found previously by Solórzano *et al.* [64]. In contrast, site  
402 based texture metric statistics did show correspondence between historical and contemporary satellite  
403 imagery. None of them were either consistent or significant. Although visual interpretation shows  
404 distinctly different canopy structures (Figure 5) the differences in how resolution is defined and issues  
405 related to image quality prevented us from quantifying these further. Unlike large scale studies  
406 by Ploton *et al.* [14] we could not scale this technique to historical data. **The successful use of our**  
**CNN classification model on a contemporary remote sensing data does suggest that texture can be**  
**used to consistently capture canopy properties 60 years apart. This suggests inflexibility on part**  
**of the FOTO technique in dealing with non-standardized data.** We advise that future valorisation  
410 efforts should preferentially work from foto negatives (if available) to ensure optimal data quality in  
411 resolution, contrast and sharpness.

412 5. Conclusion

413 Given the impact of tropical forest disturbances on atmospheric carbon emissions,  
414 biodiversity and ecosystem productivity accurate long term reporting of LULCC is an imperative.  
415 Our analysis of historical aerial survey images (1958) of the Central Congo Basin provides  
416 a window into the state of the forest at the start of the anthropocene. The use of a CNN  
417 based LULC classifier, using synthetic landscapes based image augmentation, provides a robust  
418 semi-supervised solution which scales across space and time, even for image scenes with  
419 inconsistent illumination or sharpness. Combined with contemporary remote sensing data we  
420 have shown that historical aerial survey data can be used to quantify long-term changes in LULC  
421 and AGC. We showed a shift from previously highly structured industrial deforestation of large  
422 areas for plantation purposes, to discrete smallholder clearing for farming, increasing landscape  
423 fragmentation but also opportunities for substantial regrowth. Efforts to quantify canopy texture  
424 features and their link to AGC had limited to no success. Our analysis provides insights into  
425 the rate at which deforestation and reforestation has taken place over a multi-decadal scale in the

426 central Congo basin. As such, it provides a useful historical context while interpreting past and  
427 ongoing forest research in the area.

428 **6. Additional Information and Declarations**

429 *6.1. Data availability*

430 Hufkens et al. (2019). A curated dataset of aerial survey images over the central Congo Basin, 1958.  
431 Zenodo: <https://doi.org/10.5281/zenodo.3547767>. All data not included in the latter repository can be  
432 found bundled with the analysis code as listed below. Proprietary datasets (i.e. Geo-Eye data) are not  
433 shared, but purchase order numbers allow for acquisition of these datasets to ensure reproducibility.

434 *6.2. Code availability*

435 All analysis code is available as an R / python [65] projects (<https://khufkens.github.io/orthodrc>  
436 & [https://khufkens.github.io/orthodrc\\_cnn/](https://khufkens.github.io/orthodrc_cnn/)). The analysis relied heavily on the 'raster' [66],  
437 'RStoolbox' [67], and 'landscapemetrics' [43] packages, while post-processing and plotting was  
438 facilitated by the 'tidyverse' ecosystem [68], 'ggthemes' [69], 'scales' [70] and 'cowplot' [71]. Additional  
439 plotting elements were formatted or provided by 'sf' [72] and 'rnaturallearth' [73] packages, respectively.  
440 I'm grateful for the contributions to the scientific community by the developers of these packages.

441 **Acknowledgments:** This research was supported through the Belgian Science Policy office COBECORE  
442 project (BELSPO; grant BR/175/A3/COBECORE). KH acknowledges funding from the European Union Marie  
443 Skłodowska-Curie Action (project number 797668). I'm grateful for the support of Thales de Haulleville  
444 volunteering his time in scanning the images.

445 **Author Contributions:** K.H. conceived and designed the study, analyzed the data, prepared figures, tables and  
446 authored the final draft of the manuscript. T.d.H. scanned all image data. E.K. and T.d.H. provided plot based  
447 AGC estimates. T.D., K.J., E.K, H.B., P.S., F.V.S.M., M.A., J.V.D.B., H.V and L.W. reviewed the final manuscript.

448 **Conflicts of Interest:** The authors declare no conflict of interest. The founding sponsors had no role in the design  
449 of the study; in the collection, analyses, or interpretation of data; in the writing of the manuscript, an in the  
450 decision to publish the results.

451 **References**

- 452 1. Hansen, M.C.; Potapov, P.V.; Moore, R.; Hancher, M.; Turubanova, S.A.; Tyukavina, A.; Thau, D.; Stehman,  
453 S.V.; Goetz, S.J.; Loveland, T.R.; Kommareddy, A.; Egorov, A.; Chini, L.; Justice, C.O.; Townshend,  
454 J.R.G. High-Resolution Global Maps of 21st-Century Forest Cover Change. *Science* **2013**, *342*, 850–853.  
455 doi:10.1126/science.1244693.
- 456 2. Houghton, R.A.; House, J.I.; Pongratz, J.; van der Werf, G.R.; DeFries, R.S.; Hansen, M.C.; Le Quéré, C.;  
457 Ramankutty, N. Carbon emissions from land use and land-cover change. *Biogeosciences* **2012**, *9*, 5125–5142.  
458 doi:10.5194/bg-9-5125-2012.
- 459 3. Tyukavina, A.; Baccini, A.; Hansen, M.C.; Potapov, P.V.; Stehman, S.V.; Houghton, R.A.; Krylov, A.M.;  
460 Turubanova, S.; Goetz, S.J. Aboveground carbon loss in natural and managed tropical forests from 2000 to  
461 2012. *Environmental Research Letters* **2015**, *10*, 074002. doi:10.1088/1748-9326/10/7/074002.

- 462 4. van der Werf, G.R.; Morton, D.C.; DeFries, R.S.; Olivier, J.G.J.; Kasibhatla, P.S.; Jackson, R.B.; Collatz, G.J.;  
463 Randerson, J.T. CO<sub>2</sub> emissions from forest loss. *Nature Geoscience* **2009**, *2*, 737–738. doi:10.1038/ngeo671.
- 464 5. Fauset, S.; Gloor, M.U.; Aidar, M.P.M.; Freitas, H.C.; Fyllas, N.M.; Marabesi, M.A.; Rochelle, A.L.C.;  
465 Shenkin, A.; Vieira, S.A.; Joly, C.A. Tropical forest light regimes in a human-modified landscape. *Ecosphere*  
466 **2017**, *8*, e02002. doi:10.1002/ecs2.2002.
- 467 6. Brinck, K.; Fischer, R.; Groeneveld, J.; Lehmann, S.; Dantas De Paula, M.; Pütz, S.; Sexton, J.O.; Song, D.;  
468 Huth, A. High resolution analysis of tropical forest fragmentation and its impact on the global carbon  
469 cycle. *Nature Communications* **2017**, *8*. doi:10.1038/ncomms14855.
- 470 7. Didham, R.K. Edge Structure Determines the Magnitude of Changes in Microclimate and Vegetation  
471 Structure in Tropical Forest Fragments. *Biotropica* **1999**, *31*, 17–30.
- 472 8. Laurance, W.F.; Delamônica, P.; Laurance, S.G.; Vasconcelos, H.L.; Lovejoy, T.E. Rainforest fragmentation  
473 kills big trees. *Nature* **2000**, *404*, 836–836. doi:10.1038/35009032.
- 474 9. Magnago, L.F.S.; Magrach, A.; Laurance, W.F.; Martins, S.V.; Meira-Neto, J.A.A.; Simonelli, M.; Edwards,  
475 D.P. Would protecting tropical forest fragments provide carbon and biodiversity cobenefits under REDD+?  
476 *Global Change Biology* **2015**, *21*, 3455–3468. doi:10.1111/gcb.12937.
- 477 10. Poorter, L.; Bongers, F. Leaf traits are good predictors of plant performance across 53 rain forest species.  
478 *Ecology* **2006**, *87*, 1733–1743. doi:10.1890/0012-9658(2006)87[1733:LTAGPO]2.0.CO;2.
- 479 11. Barlow, J.; Lennox, G.D.; Ferreira, J.; Berenguer, E.; Lees, A.C.; Nally, R.M.; Thomson, J.R.; Ferraz, S.F.d.B.;  
480 Louzada, J.; Oliveira, V.H.F.; Parry, L.; Ribeiro de Castro Solar, R.; Vieira, I.C.G.; Aragão, L.E.O.C.; Begotti,  
481 R.A.; Braga, R.F.; Cardoso, T.M.; Jr, R.C.d.O.; Souza Jr, C.M.; Moura, N.G.; Nunes, S.S.; Siqueira, J.V.;  
482 Pardini, R.; Silveira, J.M.; Vaz-de Mello, F.Z.; Veiga, R.C.S.; Venturieri, A.; Gardner, T.A. Anthropogenic  
483 disturbance in tropical forests can double biodiversity loss from deforestation. *Nature* **2016**, *535*, 144–147.  
484 doi:10.1038/nature18326.
- 485 12. Van de Perre, F.; Willig, M.R.; Presley, S.J.; Bapeamoni Andemwana, F.; Beeckman, H.; Boeckx, P.; Cooleman,  
486 S.; de Haan, M.; De Kesel, A.; Dessein, S.; Grootaert, P.; Huygens, D.; Janssens, S.B.; Kearsley, E.; Kabeya,  
487 P.M.; Leponce, M.; Van den Broeck, D.; Verbeeck, H.; Würsten, B.; Leirs, H.; Verheyen, E. Reconciling  
488 biodiversity and carbon stock conservation in an Afrotropical forest landscape. *Science Advances* **2018**,  
489 *4*, eaar6603. doi:10.1126/sciadv.aar6603.
- 490 13. Mitchard, E.T.A. The tropical forest carbon cycle and climate change. *Nature* **2018**, *559*, 527–534.  
491 doi:10.1038/s41586-018-0300-2.
- 492 14. Ploton, P.; Pélassier, R.; Proisy, C.; Flavenot, T.; Barbier, N.; Rai, S.N.; Couteron, P. Assessing aboveground  
493 tropical forest biomass using Google Earth canopy images. *Ecological Applications* **2012**, *22*, 993–1003.
- 494 15. Couteron, P.; Pelissier, R.; Nicolini, E.a.; Paget, D. Predicting tropical forest stand structure parameters  
495 from Fourier transform of very high-resolution remotely sensed canopy images. *Journal of Applied Ecology*  
496 **2005**, *42*, 1121–1128. doi:10.1111/j.1365-2664.2005.01097.x.
- 497 16. Barbier, N.; Couteron, P.; Proisy, C.; Malhi, Y.; Gastellu-Etchegorry, J.P. The variation of apparent crown  
498 size and canopy heterogeneity across lowland Amazonian forests. *Global Ecology and Biogeography* **2010**,  
499 *19*, 72–84. doi:10.1111/j.1466-8238.2009.00493.x.
- 500 17. DeFries, R.S.; Houghton, R.A.; Hansen, M.C.; Field, C.B.; Skole, D.; Townshend, J. Carbon emissions from  
501 tropical deforestation and regrowth based on satellite observations for the 1980s and 1990s. *Proceedings of  
502 the National Academy of Sciences* **2002**, *99*, 14256–14261. doi:10.1073/pnas.182560099.
- 503 18. Achard, F.; Beuchle, R.; Mayaux, P.; Stibig, H.J.; Bodart, C.; Brink, A.; Carboni, S.; Desclée, B.; Donnay, F.;  
504 Eva, H.D.; Lupi, A.; Raši, R.; Seliger, R.; Simonetti, D. Determination of tropical deforestation rates and  
505 related carbon losses from 1990 to 2010. *Global Change Biology* **2014**, *20*, 2540–2554. doi:10.1111/gcb.12605.
- 506 19. Ramankutty, N.; Foley, J.A. Estimating historical changes in global land cover: Croplands from 1700 to  
507 1992. *Global Biogeochemical Cycles* **1999**, *13*, 997–1027. doi:10.1029/1999GB900046.
- 508 20. Sader, S.A.; Joyce, A.T. Deforestation Rates and Trends in Costa Rica, 1940 to 1983. *Biotropica* **1988**, *20*, 11.  
509 doi:10.2307/2388421.
- 510 21. Willcock, S.; Phillips, O.L.; Platts, P.J.; Swetnam, R.D.; Balmford, A.; Burgess, N.D.; Ahrends, A.; Bayliss,  
511 J.; Doggart, N.; Doody, K.; Fanning, E.; Green, J.M.H.; Hall, J.; Howell, K.L.; Lovett, J.C.; Marchant, R.;  
512 Marshall, A.R.; Mbilinyi, B.; Munishi, P.K.T.; Owen, N.; Topp-Jorgensen, E.J.; Lewis, S.L. Land cover  
513 change and carbon emissions over 100 years in an African biodiversity hotspot. *Global Change Biology* **2016**,  
514 *22*, 2787–2800. doi:10.1111/gcb.13218.

- 515 22. Song, D.X.; Huang, C.; Sexton, J.O.; Channan, S.; Feng, M.; Townshend, J.R. Use of Landsat and  
516 Corona data for mapping forest cover change from the mid-1960s to 2000s: Case studies from the Eastern  
517 United States and Central Brazil. *ISPRS Journal of Photogrammetry and Remote Sensing* **2015**, *103*, 81–92.  
518 doi:10.1016/j.isprsjprs.2014.09.005.
- 519 23. Nita, M.D.; Munteanu, C.; Gutman, G.; Abrudan, I.V.; Radeloff, V.C. Widespread forest cutting in the  
520 aftermath of World War II captured by broad-scale historical Corona spy satellite photography. *Remote  
521 Sensing of Environment* **2018**, *204*, 322–332. doi:10.1016/j.rse.2017.10.021.
- 522 24. Buitenwerf, R.; Bond, W.J.; Stevens, N.; Trollope, W.S.W. Increased tree densities in South African  
523 savannas: >50 years of data suggests CO<sub>2</sub> as a driver. *Global Change Biology* **2012**, *18*, 675–684.  
524 doi:10.1111/j.1365-2486.2011.02561.x.
- 525 25. Hudak, A.T.; Wessman, C.A. Textural Analysis of Historical Aerial Photography to Characterize Woody  
526 Plant Encroachment in South African Savanna. *Remote Sensing of Environment* **1998**, *66*, 317–330.  
527 doi:10.1016/S0034-4257(98)00078-9.
- 528 26. Frankl, A.; Seghers, V.; Stal, C.; De Maeyer, P.; Petrie, G.; Nyssen, J. Using image-based modelling  
529 (SfM-MVS) to produce a 1935 ortho-mosaic of the Ethiopian highlands. *International Journal of Digital Earth*  
530 **2015**, *8*, 421–430. doi:10.1080/17538947.2014.942715.
- 531 27. Nyssen, J.; Petrie, G.; Mohamed, S.; Gebremeskel, G.; Seghers, V.; Debever, M.; Hadgu, K.M.; Stal, C.; Billi,  
532 P.; Demaeyer, P.; Haile, M.; Frankl, A. Recovery of the aerial photographs of Ethiopia in the 1930s. *Journal  
533 of Cultural Heritage* **2016**, *17*, 170–178. doi:10.1016/j.culher.2015.07.010.
- 534 28. Lewis, S.L.; Lopez-Gonzalez, G.; Sonké, B.; Affum-Baffoe, K.; Baker, T.R.; Ojo, L.O.; Phillips, O.L.; Reitsma,  
535 J.M.; White, L.; Comiskey, J.A.; Djuiukouo K, M.N.; Ewango, C.E.N.; Feldpausch, T.R.; Hamilton, A.C.;  
536 Gloor, M.; Hart, T.; Hladik, A.; Lloyd, J.; Lovett, J.C.; Makana, J.R.; Malhi, Y.; Mbago, F.M.; Ndangalasi,  
537 H.J.; Peacock, J.; Peh, K.S.H.; Sheil, D.; Sunderland, T.; Swaine, M.D.; Taplin, J.; Taylor, D.; Thomas, S.C.;  
538 Votere, R.; Wöll, H. Increasing carbon storage in intact African tropical forests. *Nature* **2009**, *457*, 1003–1006.  
539 Publisher: Earth and Biosphere Institute, School of Geography, University of Leeds, Leeds LS2 9JT, UK.  
540 s.l.lewis@leeds.ac.uk.
- 541 29. Butsic, V.; Baumann, M.; Shortland, A.; Walker, S.; Kuemmerle, T. Conservation and conflict in the  
542 Democratic Republic of Congo: The impacts of warfare, mining, and protected areas on deforestation.  
543 *Biological Conservation* **2015**, *191*, 266–273. doi:10.1016/j.biocon.2015.06.037.
- 544 30. Kearsley, E.; de Haulleville, T.; Hufkens, K.; Kidimbu, A.; Toirambe, B.; Baert, G.; Huygens, D.; Kebede,  
545 Y.; Defourny, P.; Bogaert, J.; Beeckman, H.; Steppe, K.; Boeckx, P.; Verbeeck, H. Conventional tree  
546 height-diameter relationships significantly overestimate aboveground carbon stocks in the Central Congo  
547 Basin. *Nature communications* **2013**, *4*, 2269. doi:10.1038/ncomms3269.
- 548 31. Lewis, S.L.; Maslin, M.A. Defining the Anthropocene. *Nature* **2015**, *519*, 171–180. doi:10.1038/nature14258.
- 549 32. Bauters, M.; Ampoorter, E.; Huygens, D.; Kearsley, E.; De Haulleville, T.; Sellan, G.; Verbeeck, H.; Boeckx,  
550 P.; Verheyen, K. Functional identity explains carbon sequestration in a 77-year-old experimental tropical  
551 plantation. *Ecosphere* **2015**, *6*, art198. doi:10.1890/ES15-00342.1.
- 552 33. Zuiderveld, K. Contrast Limited Adaptive Histogram Equalization. In *Graphics GEMs IV*; Academic Press:  
553 San Diego, CA, USA, 1994; pp. 474–485.
- 554 34. Ullman, S. The Interpretation of Structure from Motion. *Proceedings of the Royal Society of London. Series B,  
555 Biological Sciences* **1979**, *203*, 405–426.
- 556 35. QGIS Development team,. QGIS Geographic Information System., 2018. Available at: <http://qgis.osgeo.org>.
- 557 36. Ronneberger, O.; Fischer, P.; Brox, T. U-Net: Convolutional Networks for Biomedical Image Segmentation.  
558 In *Medical Image Computing and Computer-Assisted Intervention – MICCAI 2015*; Navab, N.; Hornegger, J.;  
559 Wells, W.M.; Frangi, A.F., Eds.; Springer International Publishing: Cham, 2015; Vol. 9351, pp. 234–241.  
560 doi:10.1007/978-3-319-24574-4\_28.
- 561 37. Chollet, F. Keras, 2015. Available at: <https://github.com/fchollet/keras>.
- 562 38. Yakubovskiy, P. Segmentation Models, 2019. Available at: [https://github.com/qubvel/segmentation\\_models](https://github.com/qubvel/segmentation_models).
- 563 39. Martín Abadi.; Ashish Agarwal.; Paul Barham.; Eugene Brevdo.; Zhifeng Chen.; Craig Citro.; Greg S.  
564 Corrado.; Andy Davis.; Jeffrey Dean.; Matthieu Devin.; Sanjay Ghemawat.; Ian Goodfellow.; Andrew  
Harp.; Geoffrey Irving.; Michael Isard.; Jia, Y.; Rafal Jozefowicz.; Lukasz Kaiser.; Manjunath Kudlur.; Josh

- Levenberg.; Dandelion Mané.; Rajat Monga.; Sherry Moore.; Derek Murray.; Chris Olah.; Mike Schuster.; Jonathon Shlens.; Benoit Steiner.; Ilya Sutskever.; Kunal Talwar.; Paul Tucker.; Vincent Vanhoucke.; Vijay Vasudevan.; Fernanda Viégas.; Oriol Vinyals.; Pete Warden.; Martin Wattenberg.; Martin Wicke.; Yuan Yu.; Xiaoqiang Zheng. TensorFlow: Large-Scale Machine Learning on Heterogeneous Systems, 2015. Available at: <https://www.tensorflow.org/>.
- 568 40. Kingma, D.P.; Ba, J. Adam: A Method for Stochastic Optimization. *arXiv:1412.6980 [cs]* **2017**. arXiv: 1412.6980.
- 569 41. Dice, L.R. Measures of the Amount of Ecologic Association Between Species. *Ecology* **1945**, *26*, 297–302. doi:10.2307/1932409.
- 570 42. Dale, M.R.T. *Spatial pattern analysis in plant ecology*; Cambridge studies in ecology, Cambridge University Press: Cambridge ; New York, 1999.
- 571 43. Hesselbarth, M.H.K.; Sciajini, M.; With, K.A.; Wiegand, K.; Nowosad, J. landscapemetrics: an open-source R tool to calculate landscape metrics. *Ecography* **2019**.
- 572 44. Li, B.L. Fractal geometry applications in description and analysis of patch patterns and patch dynamics. *Ecological Modelling* **2000**, *132*, 33–50. ISBN: Ecol. Model.
- 573 45. Mandelbrot, B.B. *Fractals: Form, Chance and Dimension*; W.H. Freeman and co.: New York, US, 1977.
- 574 46. Bustillo, E.; Raets, L.; Beeckman, H.; Bourland, N.; Rousseau, M.; Hubau, W.; De Mil, T. Evaluation du potentiel énergétique de la biomasse aérienne ligneuse des anciennes plantations de l'INERA Yangambi. Technical report, CIFOR, 2018.
- 575 47. Couteron, P. Quantifying change in patterned semi-arid vegetation by Fourier analysis of digitized aerial photographs. *International Journal of Remote Sensing* **2002**, *23*, 3407–3425. doi:10.1080/01431160110107699.
- 576 48. Wilcoxon, F. Individual comparisons by ranking methods. *Biometrics* **1945**, *1*, 80–83.
- 577 49. Kadmon, R.; Harari-Kremer, R. Studying Long-Term Vegetation Dynamics Using Digital Processing of Historical Aerial Photographs. *Remote Sensing of Environment* **1999**, *68*, 164–176. doi:10.1016/S0034-4257(98)00109-6.
- 578 50. Peres, C.A.; Barlow, J.; Laurance, W.F. Detecting anthropogenic disturbance in tropical forests. *Trends in Ecology & Evolution* **2006**, *21*, 227–229. doi:10.1016/j.tree.2006.03.007.
- 579 51. Verhoeven, G. BRDF and its Impact on Aerial Archaeological Photography: BRDF and its impact on aerial archaeological photography. *Archaeological Prospection* **2017**, *24*, 133–140. doi:10.1002/arp.1559.
- 580 52. Park, J.Y.; Muller-Landau, H.C.; Lichstein, J.W.; Rifai, S.W.; Dandois, J.P.; Bohlman, S.A. Quantifying Leaf Phenology of Individual Trees and Species in a Tropical Forest Using Unmanned Aerial Vehicle (UAV) Images. *Remote Sensing* **2019**, *11*, 1534. doi:10.3390/rs11131534.
- 581 53. Simini, F.; Anfodillo, T.; Carrer, M.; Banavar, J.R.; Maritan, A. Self-similarity and scaling in forest communities. *Proceedings of the National Academy of Sciences* **2010**, *107*, 7658–7662. doi:10.1073/pnas.1000137107.
- 582 54. Sole, R.V.; Manrubia, S.C. Self-similarity in rain forests: evidence for a critical state. *Physical Review E* **1995**, *51*, 6250 – 6253.
- 583 55. Hughes, M.L.; McDowell, P.F.; Marcus, W.A. Accuracy assessment of georectified aerial photographs: Implications for measuring lateral channel movement in a GIS. *Geomorphology* **2006**, *74*, 1–16. doi:10.1016/j.geomorph.2005.07.001.
- 584 56. Buscombe, D.; Ritchie, A. Landscape Classification with Deep Neural Networks. *Geosciences* **2018**, *8*, 244. doi:10.3390/geosciences8070244.
- 585 57. Gascon, C.; Williamson, G.B.; Fonseca, G.A.B.d. Receding Forest Edges and Vanishing Reserves. *Science, New Series* **2000**, *288*, 1356–1358.
- 586 58. Phillips, O.L.; Rose, S.; Mendoza, A.M.; Vargas, P.N. Resilience of Southwestern Amazon Forests to Anthropogenic Edge Effects. *Conservation Biology* **2006**, *20*, 1698–1710. doi:10.1111/j.1523-1739.2006.00523.x.
- 587 59. Reinmann, A.B.; Hutyra, L.R. Edge effects enhance carbon uptake and its vulnerability to climate change in temperate broadleaf forests. *Proceedings of the National Academy of Sciences* **2017**, *114*, 107–112. doi:10.1073/pnas.1612369114.
- 588 60. Arima, E.Y.; Walker, R.T.; Perz, S.; Souza, C. Explaining the fragmentation in the Brazilian Amazonian forest. *Journal of Land Use Science* **2015**, pp. 1–21. doi:10.1080/1747423X.2015.1027797.
- 589 61. Arima, E.Y.; Barreto, P.; Araújo, E.; Soares-Filho, B. Public policies can reduce tropical deforestation: Lessons and challenges from Brazil. *Land Use Policy* **2014**, *41*, 465–473. doi:10.1016/j.landusepol.2014.06.026.

- 621 62. Larson, A.M. Forest tenure reform in the age of climate change: Lessons for REDD+. *Global Environmental  
622 Change* **2011**, *21*, 540–549. doi:10.1016/j.gloenvcha.2010.11.008.
- 623 63. Gourlet-Fleury, S.; Mortier, F.; Fayolle, A.; Baya, F.; Ouédraogo, D.; Bénédet, F.; Picard, N. Tropical forest  
624 recovery from logging: a 24 year silvicultural experiment from Central Africa. *Philosophical Transactions of  
625 the Royal Society B: Biological Sciences* **2013**, *368*, 20120302. doi:10.1098/rstb.2012.0302.
- 626 64. Solórzano, J.V.; Gallardo-cruz, J.A.; González, E.J.; Peralta-carreta, C.; Hernández-gómez, M.; Oca,  
627 A.F.m.D.; Cervantes-jiménez, L.G.; Solórzano, J.V.; Gallardo-cruz, J.A.; González, E.J.; Peralta-carreta,  
628 C.; Hernández-gómez, M.; Oca, A.F.m.D.; Cervantes-jiménez, L.G. Contrasting the potential of  
629 Fourier transformed ordination and gray level co-occurrence matrix textures to model a tropical swamp  
630 forest 's structural and diversity attributes. *Journal of Applied Remote Sensing* **2018**, *12*, 036006.  
631 doi:10.11117/1.JRS.12.036006.
- 632 65. R Core Team. *R: A Language and Environment for Statistical Computing*; R Foundation for Statistical  
633 Computing: Vienna, Austria, 2019.
- 634 66. Hijmans, R.J. raster: Geographic Data Analysis and Modeling, 2019. Available at: <https://CRAN.R-project.org/package=raster>.
- 635 67. Leutner, B.; Horning, N.; Schwalb-Willmann, J. RStoolbox: Tools for Remote Sensing Data Analysis, 2019.  
636 Available at: <https://CRAN.R-project.org/package=RStoolbox>.
- 637 68. Wickham, H. tidyverse: Easily Install and Load the 'Tidyverse', 2017. Available at: <https://CRAN.R-project.org/package=tidyverse>.
- 638 69. Arnold, J.B. ggthemes: Extra Themes, Scales and Geoms for 'ggplot2', 2019. Available at: <https://CRAN.R-project.org/package=ggthemes>.
- 639 70. Wickham, H. scales: Scale Functions for Visualization, 2018. Available at: <https://CRAN.R-project.org/package=scales>.
- 640 71. Wilke, C.O. cowplot: Streamlined Plot Theme and Plot Annotations for 'ggplot2', 2019. Available at:  
641 <https://CRAN.R-project.org/package=cowplot>.
- 642 72. Pebesma, E. Simple Features for R: Standardized Support for Spatial Vector Data. *The R Journal* **2018**,  
643 *10*, 439–446. doi:10.32614/RJ-2018-009.
- 644 73. South, A. rnaturalearth: World Map Data from Natural Earth, 2017. Available at: <https://CRAN.R-project.org/package=rnaturalearth>.
- 645

646 © 2020 by the authors. Submitted to *Remote Sens.* for possible open access publication  
647 under the terms and conditions of the Creative Commons Attribution (CC BY) license  
648 (<http://creativecommons.org/licenses/by/4.0/>).